Biofabrication

International Society for Biofabrication

ACCEPTED MANUSCRIPT

Computer-aided patterning of PCL microspheres to build modular scaffolds featuring improved strength and neovascularized tissue integration.

To cite this article before publication: Aurelio Salerno *et al* 2022 *Biofabrication* in press https://doi.org/10.1088/1758-5090/ac7ad8

Computer-aided patterning of PCL microspheres to build modular scaffolds featuring improved strength and neovascularized tissue integration.

Aurelio Salerno,[a,*] Antonio Palladino,[a,b] Carmela Pizzoleo,[a,b] Chiara Attanasio,[a,b,*] Paolo Antonio Netti[a,c,d,*]

[a] Center for Advanced Biomaterials for Healthcare, Istituto Italiano di Tecnologia (IIT@CRIB), Largo Barsanti e Matteucci, 53, Naples 80125, Italy

[b] Department of Veterinary Medicine and Animal Productions, University of Naples Federico II, 80137 Naples, Italy

[c] Department of Chemical, Materials and Industrial Production Engineering, University of Naples Federico II, Naples 80125, Italy

[d] Interdisciplinary Research Center on Biomaterials (CRIB), University of Naples Federico II, Naples 80125, Italy

Correspondence to *:

asalerno@unina.it (Aurelio Salerno);

chiara.attanasio@unina.it (Chiara Attanasio);

nettipa@unina.it (Paolo Antonio Netti).

Graphical abstract

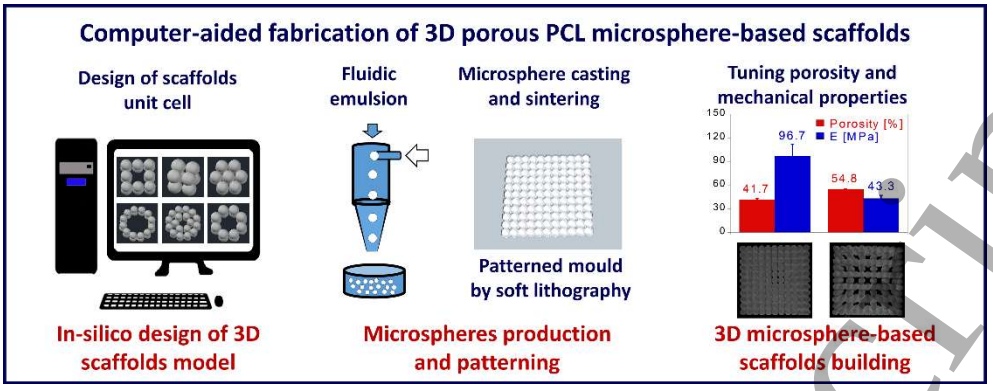

Highlights

- PCL microspheres of controlled size were prepared by fluidic emulsion.
- Soft lithography technique was used to create microsphere layers following in-silico design patterns
- A layer-by-layer approach was used to build 3D porous scaffolds featuring geometrically-inspired architectures.
- Scaffolds morphology, porosity, compression properties and biocompatibility were assayed.
- Spatial patterning of microspheres enhanced PCL scaffolds strength and enabled vascularized tissue integration.

Abstract

In the past decade, modular scaffolds prepared by assembling biocompatible and biodegradable building blocks (e.g. microspheres) have found promising applications in tissue engineering (TE) towards the repair/regeneration of damaged and impaired tissues. Nevertheless, to date this approach has failed to be transferred to the clinic due to technological limitations regarding microspheres patterning, a crucial issue for the control of scaffold strength, vascularization and integration *in vivo*. In this work, we propose a robust and reliable approach to address this issue through the fabrication of polycaprolactone (PCL) microsphere-based scaffolds with in-silico designed microarchitectures and high compression moduli. The scaffold fabrication technique consists of four main steps, starting with the manufacture of uniform PCL microspheres by fluidic emulsion technique. In the second step, patterned polydimethylsiloxane (PDMS) moulds were prepared by soft lithography. Then, layers of 500 µm PCL microspheres with geometrically inspired patterns were obtained by casting the microspheres onto PDMS moulds followed by their thermal sintering. Finally, three-dimensional porous scaffolds were built by the alignment, stacking and sintering of multiple (up to six) layers. The so prepared scaffolds showed excellent morphological and microstructural fidelity with respect to the in-silico models, and mechanical compression properties suitable for load bearing TE applications. Designed porosity and pore size features enabled *in vitro* human endothelial cells adhesion and growth as well as tissue integration and blood vessels invasion *in vivo*. Our results highlighted the strong impact of spatial patterning of microspheres on modular scaffolds response, and pay the way about the possibility to fabricate in silico-designed structures featuring biomimetic composition and architectures for specific TE purposes.

Keywords: Computer-aided design; Human endothelial cells; Modular scaffold; PCL microspheres; Soft lithography; Vascularization.

Introduction

Modular scaffolds prepared by the assembly of polymeric microspheres were deeply studied in the past decades as three-dimensional (3D) platforms for *in vitro* cell growth and *in vivo* tissue repair, with more or less success (Borden *et al.* 2004, Lu *et al.* 2003, Salerno *et al.* 2013, Salerno *et al.* 2020a, Tedesco *et al.* 2018). Microsphere-based scaffolds were designed with biomimetic morphology and mechanical behaviour optimization towards musculoskeletal tissue applications, among others (Borden *et al.* 2004; Lu *et al.* 2003, Petrie Aronin *et al.* 2009; Wang *et al.* 2009, Singh *et al.* 2010). Some examples were: poly(lactide-co-glycolide) (PLGA) scaffolds prepared by heat sintering of either porous or non-porous microspheres for *in vitro* bone cells growth (Wang *et al.* 2009); PLGA microsphere-based scaffolds prepared by compressed CO_2 sintering in presence of human umbilical cord mesenchymal stromal cells aggregates for cartilage regeneration (Singh *et al.* 2010). Besides, scaffolds prepared by sintering drug-loaded microspheres were used to enhance *in vitro* osteogenesis and chondrogenesis of cultured cells (Gupta *et al.* 2016, Shi *et al.* 2010, Wang *et al.* 2010), and to stimulate biological processes involved in new tissue development, such as vascularization and extracellular matrix (ECM) biosynthesis (Shi *et al.* 2010, Jabbarzadeh *et al.* 2012). It is worth noting that, once implanted *in vivo*, these scaffolds showed bone healing potentials and early-stage vascularization, promoting mineralized bone formation in the scaffold regions in direct contact with surrounding bone tissue (Jiang *et al.* 2010).

Computer aided design (CAD) and manufacturing processes have revolutionized the field of TE scaffolds by allowing to simultaneously process biomaterials, cells, and drugs to build patient and tissue-specific constructs with potential clinical applications (Kant and Coulombe 2018, Jacob *et al.* 2020, Liu *et al.* 2020, Matai *et al.* 2020, Salerno *et al.* 2020a, Salerno and Netti 2021). Besides, CAD processes have been recently combined with microsphere-based techniques to impart improved mechanical properties, drug delivery features and high cellular

delivery capability to the final scaffolds (Levato *et al.* 2014, Sawkins *et al.* 2015). In particular, microspheres were used as drug and/or cell delivery carriers to protect the encapsulated entity against solvents and temperature degradation during processing, together with the control of their localization and release from the scaffolds. To this purpose, drug loaded microspheres were compounded with either printable hydrogel, melted thermoplastic polymer or ceramic paste, and these mixtures were extruded through the nozzle of a bioprinter following a virtual scaffold model (Chen *et al.* 2020, Fahimipour *et al.* 2017, Li *et al.* 2021, Tarafder *et al.* 2016, Zhou *et al.* 2018). Following this approach, polycaprolactone (PCL) was loaded with PLGA microspheres carrying either vancomycin or growth factors to enhance tissue repair (Tarafder *et al.* 2016, Zhou *et al.* 2018). Similarly, cells-laden hydrogel microspheres and nerve growth factor were loaded into hydrogel paste for enhancing 3D neurite outgrowth and elongation (Chen *et al.* 2020). The versatility of this approach was demonstrated also by the work of Fahimipour *et al.* (2017) who used PLGA microspheres loaded with vascular endothelial growth factor (VEGF) in combination with a printable ceramic paste for craniofacial defects regeneration. In summary, all these approaches used nano- and microspheres as fillers to prepare drug delivery composite bioinks and to produce porous scaffold with spatiotemporal delivery of biomolecules (Tarafder *et al.* 2016). However, the combination of bioinks and delivery carriers holds certain limitations, the most important remaining the choice of biomolecules loading, plotting material and delivery carriers. For example, hydrogel bioinks ensured adequate biomolecules activity and diffusion from the carriers but, conversely, are unsuitable for *in vivo* load bearing scaffolds. Otherwise, the use of thermoplastic polymers as printing material allowed hard tissue scaffolds manufacturing but required the selection of high melting point carriers with low heat conductivity to protect the bioactivity of encapsulated growth factors (Tarafder *et al.* 2016).

Literature reporting CAD manufacturing of microsphere-based scaffolds in the absence of bioinks is scarce. Self-assembly techniques based on gravity sedimentation, mechanical vibration and capillary force were widely used in the past decades due to their ability to obtain large, colloidal crystal microsphere layers and 3D porous scaffolds with hexagonal close-packed configurations (Choi *et al.* 2009, Feng *et al.* 2019, Muto *et al.* 2009). Besides, various manipulation techniques based on electrostatic, acoustic and optical tweezers, or atomic force microscopes were used to manipulate microspheres to obtain non-colloidal crystal patterned layers (Bernassau *et al.* 2013, Hoogenboom *et al.* 2002, Li *et al.* 2010). Not so far, Rose *et al.* (2018) used flexible polymeric masks comprised of patterned openings to direct the deposition of microparticles onto various surfaces. In another work, Seul *et al.* (2008) proposed the use of surface structures, namely retaining microcavities and posts, for creating microspheres arrays. Although these techniques allowed complex microspheres layers design, they required expensive equipment, long fabrication times and their use was limited to relatively small samples.

The aim of this work was the development of a new modular approach to build microsphere-based porous scaffolds with in-silico defined microarchitectures for TE purposes. The developed approach overcomes limitations related to the use of bioinks as it involved the direct assembly and sintering of layers of PCL microspheres for 3D scaffold structure building. Microspheres layers were obtained by using patterned polydimethylsiloxane (PDMS) moulds, prepared by soft lithography, followed by thermal sintering. For 3D scaffolds building, multiple layers were aligned and stacked inside a chamber and sintered at room temperature and mild conditions upon exposure to organic solvent vapours. Different in-silico layer designs, having geometrically inspired structures, were assayed to control scaffolds morphological and architectural features and to investigate the correlation between theoretical and real scaffolds properties. Moreover, *in vitro* and *in vivo* characterization were carried out on selected samples

to evaluate scaffolds biocompatibility and integration with host tissue for possible use of these scaffolds on vascularized tissue regeneration, such as bone and osteochondral tissue.

2 Experimental

2.1 Materials

PCL (Mw = 80 KDa), polyvinyl alcohol (PVA, Mowiol® 40-88, average Mw ~205,000 g/mol), ethanol (EtOH) and dichloromethane (DCM) were purchased from Sigma-Aldrich (Milano, Italy). Polyoxyethylenesorbitan Monolaurate (Tween 20, Biochemica, Mw = 1227.72 g/m) was provided by Vetro Scientifica srl (Roma, Italy).

2.2 Modular scaffolds prepared by PCL microspheres assembly

Step 1: Fluidic device and PCL microspheres fabrication

The fluidic emulsion process used for the fabrication of PCL microspheres is shown in Figure 1 (Salerno *et al.* 2013, Pedram *et al.* 2021). The emulsion device used was assembled by using laboratory tubing and needles, while the independent control of the fluidic conditions was achieved with the aid of two syringe pumps. In particular, the continuous phase, consisting of water solution of Tween 20 (0.1 v/v%) and PVA (0.5 w/v%), was loaded into a 60-mL PE/PP syringe (Sigma-Aldrich, Milano, Italy) and pumped in a silicon tube (I.D. = 2 mm, O.D. = 4 mm, Sigma-Aldrich, Milano, Italy) by using a syringe pump (KDS 220-CE, KDScientific, Holliston, MA). Concomitantly, the dispersed phase, obtained by dissolving the PCL in DCM at RT for 4 hours, was loaded into a 2.5 mL volume Hamilton syringe (1000 series GASTIGHT®, Sigma-Aldrich, Milano, Italy) connected to a 26G blunt tip needle (Sigma-Aldrich, Milano, Italy). The needle was inserted into the silicon tube and the dispersed phase was pumped out of the needle tip by using a syringe pump (AL300-220, World Precision Instruments Company, Friedberg, Germany). Droplets of the polymeric solution formed at the needle tip and dropped into a beaker containing 100 mL of Tween 20 (0.1 v/v%) and PVA (0.5 w/v%) water solution at 190 rpm. After 3 hours of stirring under a chemical hood, samples were washed three times in distilled water to remove PVA residue. Afterward, microspheres were washed twice with ethanol, followed by air drying overnight at ambient pressure and RT under

chemical hood. The microspheres diameter (Φ) was modulated by changing the concentration of PCL in the 1-10 wt% range and the flow rate of the continuous phase (Q_{CP}) in the 4-18 mL/min range. The flow rate of the dispersed phase (Q_{DP}) was fixed to 90 μL/min for all the tests.

Step 2: Patterned PDMS moulds preparation by soft lithography

The patterned PDMS (Sylgard 184, Dow Corning, USA) moulds used to prepare the microspheres layers were provided with ordered arrays of vertical pillars with different diameters and spacing. The PDMS moulds were obtained by a replica moulding process and by using 4 mm-thick polymethyl methacrylate (PMMA) sheets (Goodfellow Cambridge Limited, England) processed by micromilling machine (Minitech Machinery Corporation, Norcross, GA, USA) equipped with two-flute end mills (Performance Micro Tool, Janesville, WI, USA) to fabricate the master (Salerno *et al.* 2020b) (Figure 1). An array of cylindrical cavities was obtained by drilling PMMA sheets with cylindrical tips having a diameter varying from 70 μ up to 500 μm, depending on the array design. The spindle speed was set to 10.000 rpm while the feed rate was set to 20 mm/min for all the experiments. To obtain the PDMS moulds, a 10/1 (w/w) PDMS base/curing agent mixture was poured onto the fabricated PMMA masters and the system was degassed to remove entrapped air bubbles and completely fill the holes. Once completed the air bubbles removal, the PDMS mixture was cured in an oven at 80°C for 2 hours to obtain the final microspheres alignment moulds. Layers morphology and microstructural parameters were controlled by designing PDMS moulds with different microspheres alignment patterns and presenting spacers as void generating elements.

Step 3: microspheres layers preparation by mould patterning and melt sintering

To prepare the microspheres layers with pre-defined patterns, the PCL microspheres produced by the fluidic emulsion process were arranged into patterned PDMS moulds with pre-defined arrays of vertical pillars. PCL microspheres measuring 500 μm in diameter were poured

onto the mould, and a drop of EtOH was dropped onto the microspheres. This EtOH wetting was performed to overcome microspheres repulsion problems as a consequence of static electricity. Moreover, the EtOH promoted microspheres ordering into the mould cavities due to the density difference between EtOH (0.789 g/cm^3) and PCL (1.145 g/cm^3). The excess of microspheres was rapidly removed from the top of the mould with the aid of tweezers and the array checked with the aid of a stereomicroscope (Olympus SZX16), that helped us to control that each position was filled by the microspheres. The entire process required less than 5 minutes/layer to complete. Then, the moulds containing the microspheres were placed under moderate vacuum to accelerate EtOH evaporation before thermal sintering. As shown in the Step 3 of Figure 1, the final PCL microsphere layers were obtained by thermal sintering. To this purpose, we studied the optimization of temperature and time pairs to prepare 500 µm PCL microspheres layers. In particular, the temperature was varied in the 62 to 64ºC range, while processing time was studied in the 5 to 60 minutes interval. Optimal sintering temperature and time pair was 64ºC and 7 minutes and, these parameters were suitable for all the different designs used in this work.

Step 4: 3D porous scaffolds by layers assembly and vapour sintering

The last step used for the fabrication of 3D scaffolds involved the alignment of the previously formed layers and their sintering. As shown in Figure 1, six layers were aligned in a PDMS chamber with size and geometry fitting the size, border and height of the overlapped layers, and the system was closed with a glass slide on the top. Sintering was carried out by using a vaporization setup consisting of a 100 mL glass conical flask equipped with a top two-hole rubber cork. The first hole was used as the entrance of the purging nitrogen (N_2) at 0.15 bar pressure through a Pasteur pipette whose tip was immersed into a 2 mL of a 30/70 v/v DCM/EtOH mixture dispensed at the bottom of the flask. The second hole of the cork was connected to a polytetrafluoroethylene (PTFE) tube having internal and external diameters of 1

mm and 1.5 mm, respectively. The tube was connected to a bifurcating chamber, made of PDMS sealed with a glass slide, that provides the solvent mixture vapours flow into two PTFE tubes connected to one of the entrances of the layers alignment chamber previously described. Sintering was carried out by processing the layers with vapours for 2 minutes on each side. After sintering, samples were left under chemical hood for 10 minutes, extracted from the aligning chamber, washed in pure EtOH twice and leaved under chemical hood for 24 hours to remove the remaining DCM.

2.4 Morphological and microstructural characterization

The morphology of the different samples, e.g. PCL microspheres, PCL layers and porous scaffolds, was evaluated by stereomicroscope imaging and scanning electron microscope (SEM, Ultraplus, Zeiss, Germany) analysis. For SEM analysis, sample's surface and cross-section were gold sputtered using a sputter coater (208HR, Cressington, UK) and analysed at an accelerating voltage of 10 kV. The mean diameter (Φ) and diameter distribution of the PCL microspheres were assessed by Image analysis (Image J®). Image analysis was carried out on 2X stereomicroscope images of about one hundred microspheres for each condition. The acquired images of the microspheres were analysed using the ''particle analysis'' tools of the Image J® software pack and the diameter was then calculated from area measurement (Pedram *et al.* 2021). X-ray computed tomography (MicroCT, Bruker Skyscan 1172, Milan, Italy) was used to assess the overall porosity and microstructural properties of the scaffolds (Salerno *et al.* 2020b). Measurements were performed at a voltage of 40 kV, 250 µA current and 3.5 µm pixel size. The transmission images were reconstructed using Skyscan NRecon software and further analysed by CTAn software package. MicroCT equipment was also used to assess the static compression properties of the scaffolds on both transversal and aligned directions to the scaffold's layers. The scaffolds, measuring 5.5 mm in size and 3 mm thick (cubic geometry, 6-layers), were tested by using a Skyscan material testing stage (V1.1) equipped with a load cell

of 220 N and that contains all the necessary parts to apply a compression load to the scaffolds and to measure the applied force and displacement. The scaffolds were placed onto the lower plate that moves up at a crosshead speed of 0.4 mm/min until a maximum displacement of 5.5 mm. Before the test, a small pre-load was applied to the scaffolds to ensure the close contact between scaffold surfaces and bottom and top plates. The scaffolds were continuously compressed until the achievement of the limit of the load cells or when the compression induced excessive samples breaking and the consequent drop of the measured force. The force vs. displacement data were acquired and converted into stress (σ) and strain (ε) data to obtain the σ vs. ε curve of the different scaffolds. The elastic modulus (E) was then determined as the slope of the linear portion of the σ vs. ε curve. At the end of the compression tests, samples were maintained compressed between the plates and MicroCT was used to analyse the 3D structure of the samples and the resulting porosity and pore size distribution, as described previously. Five samples were tested for each scaffolds type.

2.5 *In vitro* cell-material interaction

In vitro culture tests were carried out on 3-layers cubic IP scaffolds (5.5 mm side, 1.5 mm thick) with or without NaOH treatment to assess biocompatibility properties. The NaOH treatment was carried out by soaking the scaffold in a solution of NaOH (0.1 M) and EtOH in a 1:1 ratio, for 15 min at 37 ºC. Both treated (+ NaOH) and untreated (- NaOH) scaffolds were sterilized via UV exposure for 1 hour (30 min + 30 min each side). Scaffolds were seeded in a 48 low attachment well plate with 1 x 10^4 human umbilical cord vein cells (HUVECs) (Lonza, Basel, Switzerland) at passage 3, suspended in a 40 µl drop of culture medium. After cell adhesion (1 hour post-seeding), the cell/scaffold constructs were moved to another 48 low attachment well plate and 60 µl of culture medium were added to each well for *in vitro* culture. Experimental endpoints were set at 6 hours, 1 day, 3 days, 7 and 11 days of culture. Cells were cultured in M200 (Thermo-Fisher) culture medium integrated with Low Serum Growth

Supplement Kit (Thermo-Fisher) and 20% fetal bovine serum (Sigma-Aldrich). At each endpoint, to assess the number of viable cells onto the scaffolds, a cell viability test was performed by PrestoBlue Assay (Invitrogen), that enabled the online monitoring of cell proliferation (Sonnaert *et al.* 2015). The assay was carried out according to the manufacturer's protocol. Briefly, 100 µL of PrestoBlue solution (10% in medium without serum and phenol red) were added to each well containing cell/scaffold constructs and the samples were incubated at 37 °C for 1 hour to promote the nonfluorescent blue resazurin reduction to the fluorescent pink resorufin. The solution was subsequently transferred to a new well in 96-well plate, and the change in the fluorescence of the test reagent was measured using a spectrophotometer (Perkin Elmer, Italy) at wavelengths 600 nm following Presto Blue provider instructions. The number of viable cells was assayed by comparing fluorescence values with those of the calibration curve obtained by the correlation between a known cell number into the 48-well culture plates and the correspondent fluorescence value. Three samples were analysed for each scaffolds type. Cell morphology and colonization were investigated by using confocal laser scanning microscopy (CLSM) analysis. The cell/scaffold constructs were washed with phosphate buffer solution (PBS) and fixed with 4% v/v paraformaldehyde at 4 °C for 2 hours. Samples were then washed three times with PBS solution and incubated with Triton 0.2% v/v for 5 min at RT. Subsequently, the constructs were washed three times with PBS and incubated with blocking buffer containing 3% w/v bovine serum albumin and 3% v/v fetal bovin serum in PBS for 1 hour at RT. Actin was stained with Phalloidin-488 (1:200 diluted in blocking buffer) for 40 minutes at RT. Samples were then washed three times with PBS and nucleus was stained with DRAQ5 (1:1000 diluted in PBS) for 20 min at RT. The as obtained cell/scaffold constructs were washed three times with PBS and characterized by CLSM (Leica TCS SP5 II, Italy) to evaluate HUVECs adhesion and morphology.

2.6 *In vivo* study

In vivo experiments were performed in accordance with the Directive 2010/63/EU. All animals were housed one per cage with free access to water and food. BALB/c female mice 6-8 weeks of age were used for the study. Scaffolds were 6-layers cubic shaped (5.5 mm side, 3 mm thick) with LP and IP configuration without NaOH treatment. The samples were implanted in a subcutaneous pocket model. After 21 days animals were sacrificed by administering a lethal dose of anaesthetic and perfused with a contrast agent. Afterwards, scaffolds were retrieved and processed for MicroCT analysis as previously described (Palladino *et al.* 2021). Subsequently, the samples were cut into 10 µm thick slices by using a cryostat (SLEE MEV, Mainz, Germany), stained with Hematoxylin-Eosin following standard protocol and observed by means of an optical microscope (Olympus BX53) to assess the degree of scaffold integration with the host tissue.

2.7 Statistical analysis

The statistical significance of the results was assessed by one-way analysis of variance (ANOVA) and Tukey post-hoc test at the significance level $p<0.05$.

3 Results

3.1 PCL microspheres fabrication by fluidic emulsion

In this work, we implemented a fluidic emulsion process (Step1, Figure 1) suitable for the fabrication of PCL microspheres with variable Φ and narrow distributions starting from PCL solutions in DCM (Figures 2 and S1). Moreover, the optimization of microspheres properties was achieved by studying the effect of PCL concentration, in the 1-10 w% range, and Q_{CP} in the range of 4-18 mL/min, on Φ, while fixing Q_{DP} to 90 µL/min. In agreement with other studies (Choi *et al.* 2009, Salerno *et al.* 2013, Pedram *et al.* 2021), Φ decreased with decreasing total polymer concentration and with increasing Q_{CP} (Figure 2A). In particular, at 1 w% solution, Φ varied from 178.5 ± 12.9 µm for Q_{CP} = 4 mL/min, to 122.4 ± 8.0 µm for Q_{CP} = 18 mL/min; at 4 w% Φ varied from 360.0 ± 3.3 µm for Q_{CP} = 4 mL/min, to 212.4 ± 4.0 µm for Q_{CP} = 18 mL/min; at 10 w% Φ varied from 648.0 ± 5.7 µm for Q_{CP} = 4 mL/min, to 431.0 ± 4.5 µm for Q_{CP} = 18 mL/min. SEM microscopy allowed to study the morphology of the surface and cross-section of the PCL microspheres. As shown in Figures 2B and C, the surface morphology of the microspheres was dependent on the crystallization behaviour of PCL, that starts from the nucleation sites and proceeds with a radial growth, leading to the formation of spherulites composed by crystalline lamellae (Causa *et al.* 2015). Such morphology was determined by the impingement of adjacent spherulites that therefore appeared flat and sharp-edged. SEM observation of the cross-section of the microspheres, reported in Figure 2D, also showed the absence of porosity within the microspheres, as a consequence of the slow DCM diffusion from the droplet to the coagulation medium.

3.2 PCL microsphere-sintered layers design and morphology

PCL microsphere-sintered scaffolds were fabricated by a three-steps process that involved the design of the virtual models, the fabrication of the sintered layers and, finally, the layer-by-layer scaffolds building.

Pictures of the virtual models of the different layers were reported in Figure 3 while the SEM morphology of the obtained samples were shown in Figure 4. As shown in Figure 3, by using soft lithography we modulated the two-dimensional non-close-packed colloidal crystal arrays following geometrically inspired patterns. These include square patterns, where the microspheres centres were located either into three or four corners of a 500 μm side square; hexagonal closed-packed pattern and patterns obtained by placing microspheres centres into the corners of octagonal and dodecagonal design as well as their combination. Noteworthy, the integrity of the layers required fixing adjacent microspheres centres distance equals to Φ, that was 500 μm in this study, and ensuring the formation of closed geometries. The SEM images of the layers, reported in Figure 4, provided important information regarding the morphological properties of the samples and their fidelity with the virtual counterparts showed in Figure 3. In the case of the hexagonal array (Figure 4A), each PCL microsphere with an average diameter of 500 μm ca. contacts with six adjacent microspheres. After thermal sintering, the morphology of the microspheres remained spherical with slight flatting of the top portion in contact with the cover glass. The high magnification of Figure 4B demonstrated the formation of wide strong connecting necks between adjacent microspheres. As a direct consequence, layers were easily removed from the PDMS mould and manipulated further for scaffold building. In the case of hexagonal layer, samples were characterized by a monomodal pore size distribution, with small (Type I) circular pores well matching the size and shape of inter-particle pores of a colloidal microsphere array in hexagonal lattice structure. Similar results, in terms of particles morphology and sintering, were observed for samples prepared by using microspheres arrays of square, octagonal, dodecagonal and combined designs of Figures 4C-K. We may therefore conclude that this mould pattering strategy enabled manufacturing layers without the need to adjust melt sintering parameters to different layer designs. Morphological analysis also indicated that the hexagonal and square configurations provided monomodal pores size

distributions, with pore size that increased from 70 to 200 μm, according to 500 μm microspheres inter-particles space. The in-silico design of microsphere sintered layers following different geometrically-inspired arrays resulted in layers with bi-modal (octagonal) or evenly tri-modal (dodecagonal with/without hexagonal) pore sizes (Figures 4D-K).

3.3 3D PCL scaffolds morphology and microarchitecture

Porous 3D microspheres-sintered scaffolds were fabricated by layers alignment, stacking and sintering (Step 3, Figure 1). As shown in the SEM images of Figures 5A-F, all the scaffolds have a microspheres-sintered morphology were the size and shape of each microsphere were similar to those observed for the starting layers (Figure 4). Most importantly, all the scaffolds have aligned pores in the direction transversal to the layers plane, while scaffolds morphology and pore structure features were directly dependent on the layers design features. For example, the pre-defined removal of microspheres from cubic-shape unit cell scaffolds enhanced both scaffolds porosity and pore size (compare Figures 5A and B) without affecting samples integrity. More complex scaffold structures characterized by pores having different size scales and spatial distribution were also obtained by assembling layers with more complex geometries (Figures 5C-F). SEM micrographs of the lateral surface of octagonal scaffold, shown in Figures 5G and H, demonstrated the good alignment of the layers as well as the strong sintering achieved by the solvent vapour treatment. Besides, the morphology and size of scaffold pores was preserved while the necks between adjacent microspheres have a size and morphology similar to the necks achieved by temperature treatment (Figure 5H). Most notably, the solvent vapour treatment provided sintering into the inner region of the scaffolds (Figure 5K), even if this result was to some extent affected by the uncontrolled presence of non-contact points between aligned microspheres of adjacent layers (not shown).

The reconstructed 3D images of PCL scaffolds prepared as a function of layer design were shown in Figure 6 while comparison between in-silico values and measured values of

porosity and mean pores size were reported in Table 1. MicroCT enabled the visualization of the 3D architecture of the scaffolds and therefore demonstrated the excellent correlation with their in-silico counterparts. All the scaffolds have aligned and fully interconnected pores on both axial and transversal directions to the layer plane, scaffolds edges varied depending on layers design, being planar for the square geometry while more irregular for the others designs (Figure 6). Furthermore, by modulating the unit cell features, PCL scaffolds of different porosity and pore size were obtained (Table 1). In particular, the lowest porosity values (as measured by gravimetric tests), equal to 38.4 ± 1.1 % and 41.7 ± 1.3 %, were obtained for the scaffolds having hexagonal configuration and square configuration with the microsphere's centres located onto four corners, respectively. The other samples have porosity values in the range from 46.7 ± 0.8 % for the square configuration with the microsphere's centres located onto three corners, up to 67.6 ± 1.4 % of dodecagonal configuration (Figure 3D). These results were confirmed by MicroCT measurements (not shown) and showed a slight (5-12%) porosity decrease if compared to theoretical values, probably due to the flattening of the layers and the bonding process. In agreement with SEM results, the choice of the different design also affected the size of the pores of the scaffolds, as measured by Image analysis. Depending on the chosen microspheres arrays, we identified three main pore size types: (I) smaller, equal to 70-80 µm; (II) intermediate, equal to 200-210 µm and (III) large, equal to either 500-600 µm, 800 µm, or 1400 µm (Table 1). In conclusion, by simply changing microspheres layer design it was possible to adjust the values of porosity and pore size distribution, in the ranges of 38 to 64% and 70 to 1400 µm, respectively, while ensuring full pores interconnectivity to meet microarchitectural requirements of TE applications.

3.4 3D PCL scaffolds static compression properties

Further work was carried out to validate the mechanical consistency of the scaffolds. To this purpose, we selected the two cubic-shaped designs of Figures 6A and E as they provided a

simple and efficient way to modulate scaffolds porosity and pores size in ranges suitable for TE purposes, by simply reducing the microspheres coordination number and without altering their overall size and external geometry. Furthermore, these samples have planar lateral surfaces and were those selected for the biological characterization. As shown in Figure 7, mechanical compression properties of PCL scaffolds were significantly dependent on both layers design and testing direction. The highest value of E, equals to 96.7 ± 15.2 MPa, was obtained for the low porosity scaffold (LP, Figure 6A) tested along layers direction (z-axis). This scaffold evidenced a significant decrease (44%) of E when tested transversally to the layers plane (x-axis, Figure 7B). A similar behaviour was observed for the scaffold with intermediate porosity value (IP, Figure 6E), while in this case the E values decreased from 43.3 ± 3.3 MPa (x-axis) down to 33.7 ± 6.9 MPa (z-axis) (22%). Accordingly, the transition from elastic to plastic deformation of IP scaffolds occurred at lower yield strengths if compared to LP ones (σ_Y = 4.15 ± 0.46 MPa and 3.27 ± 0.62 MPa in the z-axis and σ_Y = 5.65 ± 0.93 MPa and 1.56 ± 0.44 MPa in the x-axis for LP and IP scaffolds, respectively). This change in the elastic-to-plastic transition point can be better understood by the analysis of the 3D images of the compressed scaffolds obtained by MicroCT analysis and depicted in Figures 7C-F. The LP scaffolds tested transversally to the layers plane (z-axis) retained the 3D architecture until the achievement of the limit of the load cell (220 N) (Figure 7C). Conversely, the IP scaffolds significantly collapsed under compression and we observed the slip between adjacent layers due to the brake of the neck created by solvent vapour sintering (blue curve of Figure 7A and 3D image of Figure 7D). Both scaffolds' types tested along the x-axis experienced an abrupt decrease of the mechanical behaviour once exceeded the elastic limits due to the occurrence of massive layers debonding and/or samples bending (Figures 7E and F). Figure S2 compared the porosity, mean pore size and pore size distribution of LP and IP scaffolds and, also showed the effect of mechanical compression in the case of LP scaffolds teste along z-axis, as assessed by MicroCT

analysis. The effect of compression on IP scaffolds is not shown as these scaffolds experienced microsphere necks rupture at the end of the test. As shown in Figure S2A, the porosity and the mean pore size increase from 40.1 ± 0.8 % and 215.9 ± 16.1 μm for LP scaffold up to 53.0 ± 0.6 % and 351.8 ± 11.0 μm for IP scaffold, respectively. The LP scaffolds after compression evidenced the decrease of both porosity and mean pore size down to 32.9 ± 1.8 % and 176.3 ± 11.9 μm, respectively. Most notably, the pore size distributions of the LP and IP scaffolds reported in Figure S2B evidenced two main peaks: a low mean pore size value of 190 μm for both scaffolds and a high mean pore size value of 320 μm for LP scaffolds and 550 μm for IP scaffolds. After compression, the high mean pore size peak value of LP scaffolds shifted down to 260 μm, while the low peak remained almost unchanged. These double peaks of the LP scaffolds are ascribable to the size of the pores of the cubic cell unit as well as to the presence of microspheres sintering defects between adjacent layers, that almost disappeared after compression. The IP scaffolds pores well replicated the structural features of the virtual scaffold model of Figure 3, that have 200 and 500 μm pores in the axial and transversal layer directions.

3.5 *In vitro* and *in vivo* 3D PCL microsphere-sintered scaffolds characterization

In vitro cell culture experiments were carried out to assess the biocompatibility of the scaffolds as well as their suitability to sustain cell adhesion, proliferation, and migration as pre-requisites before validation in the preclinical setting. The tests were carried out by statically seeding HUVECs onto the surface of PCL scaffolds having cubic-shape layers geometry and LP configuration. The IP samples were excluded from this test as the large pores would have facilitated the fast diffusion of cell suspension during static seeding, finally limiting cell seeding efficiency. PrestoBlue assay results displaying viable cells over time were reported in Figure 8. After 6 hours from seeding, the number of viable cells adherent onto the + NaOH scaffolds, equals to 5925 ± 560, was twice than that of untreated ones (- NaOH), equals to 2942 ± 528 ($p < 0.05$) as shown in Figure 8A. As culture time increased, we observed the progressive decrease

of the differences on viable cell number between untreated (- NaOH) and treated scaffolds (+ NaOH) while, at day 11 post-seeding, both scaffolds showed similar viable cell number (6833 ± 672 for -NaOH and 8477 ± 1376 for + NaOH). As expected, the highest cell adhesion and proliferation phenomena were observed for the CTR, with the HUVECs that duplicated their number in 2.5-3 days approximately (Figure 8A). Interestingly, when the number of viable cells onto the scaffolds was normalized to the number of adherent cells (values at 6 hours), the scaffolds displayed a similar cell number at early time points (1 and 3 days), while at 7 and 11 days of culture untreated scaffolds displayed a higher cell number than + NaOH samples. Data reported in Figure 8B also confirmed that HUVEC proliferation activity was highest on the CTR. Actin cytoskeleton and nuclei were stained to visualize and assess cell morphology and adhesion on the scaffolds. As shown in Figures 8C and D, the HUVECs were well attached to the scaffold surface and displayed a flat and stretched morphology onto the microsphere surface and in the neck between adjacent microspheres, respectively. These results indicated good cellular interaction with the supporting scaffold structure. As shown in Figure 9A, both scaffolds promoted the growth and development of new blood vessels inside the porous structure while the vascularization of the IP scaffolds was higher than that of LP, even if this difference was not statistically relevant ($p < 0.05$). The results of these measurements were normalized to the vessel volume measured near the implant to take into account the differences of the regional vascularization at the implantation site. As expected, the amount of blood vessels inside the scaffolds was higher in the region close to the main blood vessels of surrounding tissue and decreased about to a half in the other two regions for both scaffold configurations (Figure 9B). The average vessel diameter distribution inside the scaffold was also assessed with the 3D analysis tools of the CtAn software. As shown in Figure 9C, more than 70% of blood vessels were in the 5 to 65 μm range for both scaffold types, and minor differences were observed in the distribution histograms of LP and IP scaffolds.

The two types of square-shape microspheres-sintered scaffolds tested in this work, namely LP and IP, have respectively 40 and 53% porosity, 200 and 600 µm pore sizes and fully interconnected aligned pores (Figures 3 and 6). These microarchitectural features enabled cells and tissue growth into the scaffolds pores (Figure 9D-F), and the development of a stable vasculature connected to the animal's cardiovascular system after three weeks of implantation in subcutaneous mice pocket.

4 Discussion

This study demonstrated that the computer-aided patterning of PCL microspheres following geometrically inspired designs enabled to build 3D porous scaffolds with architectural features and mechanical strength suitable to promote *in vitro* cell adhesion and proliferation as well as *in vivo* neo-tissue integration. As shown in Figure 1, the fabrication of the scaffolds required the preparation of PCL microspheres with highly controlled Φ and spherical shape in order to fit the position of the PDMS moulds. To achieve this aim, we developed a fluidic emulsion process starting from PCL solutions in DCM and adjusting the Q_{CP} to obtain microspheres with Φ in the range of 100-600 μm as this dimensional interval is considered suitable for the preparation of TE scaffolds (Shi et al. 2010, Wang et al. 2010, Gupta et al. 2016). There is wide scientific literature that described the mechanisms involved during the formation of droplets by fluidic emulsion. For example, it was reported that, in the case of dripping regime, droplets of the dispersed phase generated at the tip of the needle when the shear stress imposed by the continuous phase overcome viscosity and surface tension forces and break-up the fluid bed (Watanabe *et al.* 2011, Moon *et al.* 2014). As a direct consequence, the increase of Q_{CP} increases the shear stress to the dispersed phase, accelerates droplets formation and, ultimately, lead to the decrease of Φ (Watanabe *et al.* 2011, Moon *et al.* 2014). Besides, the effect of polymers concentration is more complex as polymeric solution concentration affects not only the viscosity of the solution but also alter the interfacial tension between the two solutions. For example, as the solution concentration increased, the viscosity increased too, finally leading to larger droplets and, then larger microspheres (Figures 2 and S1). Concomitantly, higher polymer concentrations accelerated supersaturation and droplets solidification with the consequent decrease of droplets shrinkage and the formation of larger microspheres (Watanabe *et al.* 2011). For the samples prepared at Q_{CP} = 8 mL/min and polymer concentration of 10 w%, the diameter of the droplets generated at the needle tip was about twice

the diameter of resulting microspheres (1100 μm approximately, data not shown), therefore supporting the choice of a silicon tube with 2 mm ID for the fluidic device assembly. Results of Figure S1 corroborated these considerations and also evidenced the narrow (10% coefficient of variation) Φ distribution of the different batches. These results suggested that the choice of the fluidic emulsion enabled excellent control of Φ distribution of PCL microspheres in the 100-600 μm range.

The engineering of microsphere-based scaffolds with in-silico designed architecture was achieved by a layer-by-layer approach and required the fabrication of PCL microsphere sintered layers by using patterned PDMS moulds prepared by soft lithography (Step 2 of Figure 1). The basic principle of microspheres patterning was to fabricate arrays of vertical pillars able to fix each microsphere into a position defined following the virtual scaffolds model. Although by micromilling and replica moulding processes it would be possible to obtain every kind of patterned microspheres layers, it is worth to note that layer's configurations were chosen taking into the account three main fundamental aspects of developed process. First, as previously noted, layers integrity and stability required the close contact between adjacent microspheres together with the presence of closed geometries to reduce possible deformation. Subsequently, the patterns must provide the possibility to modulate final scaffolds morphology and microstructural features, namely porosity and pore size, that are difficult to be achieved by colloidal arrays. Finally, the array must provide adequate layer features uniformity and symmetry. All these characteristics were fully matched by choosing geometrically-inspired patterns, such as those tested and showed in Figure 3, and by the optimization of layers sintering. The first attempts to optimize microspheres sintering were carried out by preparing two patterned PDMS moulds featuring square configuration with the microsphere's centres located onto four corners (first column of Figure 3), and with pillars spacing to accommodate PCL microspheres with Φ of either 200 or 500 μm. The results of these tests (not shown)

indicated that 200 µm microspheres were inadequate to fill all of the position of the array by manual handling. On the contrary, the largest microspheres easily distributed following the underlying pattern, aided by the PCL/EtOH density difference and fast sedimentation. Optimal thermal sintering conditions of 500 µm PCL microspheres layers were 64 ºC and 7 minutes and, these parameters were suitable for all the different designs used in this work (Figure 4). Microspheres sintering depended on the motion of polymeric chains from the microspheres surface to contact points that leads to polymeric chain inter-diffusion and the subsequent formation of connecting necks between microspheres (Borden *et al.* 2003, Luciani *et al.* 2011). Our results were in agreement with previous works reporting a sintering temperature in the 60 to 65 ºC range for PCL microspheres prepared by emulsion techniques (Khoshroo *et al.* 2017, Luciani *et al.* 2011, Shahin-Shamsabadi *et al.* 2018). Most notably, the flat geometry of the layers promoted the uniform heat transfer from the top (glass slide cover) to the underlying microspheres and enabled to complete samples sintering in a time period one order of magnitude lower than those reported in other works (Khoshroo *et al.* 2017, Luciani *et al.* 2011, Shahin-Shamsabadi *et al.* 2018). Processing techniques for patterning micro/nanospheres in two-dimensional arrays often rely on self-organization principle, that offer a high processing speed but were limited to hexagonal layer morphology (Bernassau *et al.* 2013, Hoogenboom *et al.* 2002, Li *et al.* 2010]. Literature studies regarding the use of patterned PDMS moulds to control the planar organization of microspheres is scarce. In the work by Li *et al.* (2010), PDMS moulds were used to lift up 2D self-assembled close-packed colloidal microspheres arrays that were then deformed by solvent swelling or mechanical stretching to adjust the lattice structures. Using this method, authors tuned the interparticle distance and modulated the lattice structure of 560 nm particles, while no information were provided about the scalability of the approach to micrometric size particles and the possibility to obtain sintered layers. Further interesting microspheres patterning techniques were the screen printing method described by Rose *et al.*

(2018) used to create arrays of microparticles onto different substrates, as well as the use of infrared femtosecond pulses to the selective removal of individual silica microspheres within ordered lattices (Cai and Piestun 2006). If compared to previously described approaches, the patterned PDMS mould method herein reported has a low level of automation while its versatility may enable achieving evenly complex designs and materials assembly. The final 3D scaffolds fabrication step (N°4 of Figure 1) involved the alignment, stacking and sintering of PCL microspheres layers. The process was carried out within a PDMS chamber fabricated by soft lithography and capable to process up to six layers. In this case, sintering was carried out by treating the layers with vapours of a 30/70 DCM/EtOH mixture flowing with the aid of N_2 jet through four windows of the PDMS chamber. Mixing DCM (PCL solvent) and EtOH (PCL antisolvent) provided enhanced control over polymer plasticization. As the layers were inserted all at once in the PDMS chamber and subjected to a moderate compression, the plasticizing vapour mixture plasticized the polymeric microspheres at the contact points and promoted the formation of the neck between contacting microspheres of the adjacent layers (Figure 5). Most notably, the short treatment time (2 minutes per side) and the room temperature enabled strong layers bonding without significantly affecting layers morphology and microstructure. There are several recent works reporting the fabrication of 3D scaffolds by layers stacking and sintering (Gallego *et al.* 2008, Rossi *et al.* 2016, Sodha *et al.* 2001, Tang *et al.* 2020, Zieber *et al.* 2014). For instance, Gallego *et al.* (2008) have presented a multilayer micromolding technique to fabricate 3D porous scaffolds by the manual stacking of 10 µm thick PCL layers followed by thermal bonding at 90 ºC and 52 psi for 2 minutes. A similar approach was used by Sodha *et al.* (2011]) that manually stacked and aligned PCL layers in ethanol followed by sintering at 40 ºC and 85 psi for 20 minutes. Main limitations of these approaches were the difficult control of layers alignment together with the fact that scaffold consistency depended on the size of the microstructures, the size of the samples and the stiffness of the polymeric layers (Gallego *et al.*

2008, Sodha *et al.* 2011). As demonstrated by the morphological (SEM) and microstructural (MicroCT) results showed in Figures 5 and 6, respectively, the use of PDMS moulds ensured proper layers alignment and reliability of scaffolds features. Even if in this work we did not loaded drugs into the scaffolds, our choice of the solvent vapour mixture sintering, instead of the temperature one, rely on the fact that by this way we can possibly preserve the bioactivity of drug delivery carriers loaded within the scaffolds during the layer's alignment step. This consideration is in agreement with recent works on the plasticization of drug-loaded carriers by vapour mixtures of EtOH and dimethyl carbonate (de Alteriis *et al.* 2015) as well as PLGA layer to build 3D scaffolds (Ryu *et al.* 2007). Nevertheless, suitable alternative treatments for layers sintering can be that employing compressed fluids, namely CO_2 and N_2 that were not so far used to sinter PLGA layers having the dimensions of 10 mm side and 60 μm thick with or without seeded cells (Yang *et al.* 2005, Xie *et al.* 2009). As shown in Table 1, the porosity and pore size features of the PCL scaffolds can be modulated from 38.4 ± 1.1 % up to 67.6 ± 1.4 % and from 76.9 ± 1.8 μm up to 1373.5 ± 14.9 μm, respectively, without affecting the interconnectivity of the pores. However, all of the scaffolds have similar pores size in the direction parallel to the layer plane, equals to 150 μm ca., because of the size of the microspheres and their alignment along the transversal direction. The mechanical parameters herein obtained for the cubic-shaped PCL scaffolds of Figures 3A and 3E were lower than those of bulk material (E of PCL equals to 300 MPa and σ_y equals to 10-12 MPa), but significantly higher than those reported in other works for PCL microspheres sintered scaffolds having random microspheres distribution (Khoshroo *et al.* 2017, Luciani *et al.* 2008, Luciani *et al.* 2011). Overall, reported values of E for PCL microspheres scaffolds having 40% porosity were between 15 and 30 MPa and between 15 and 20 MPa for melt and solvent sintering, respectively (Khoshroo *et al.* 2017, Luciani *et al.* 2008, Luciani *et al.* 2011). The increase of E for the ordered scaffolds of this work is ascribable to the alignment of the microspheres and the

compression axis that induced microspheres compression along their centre's direction, limiting the shear stresses imposed to the sintering necks. However, when the compression exceeded the elastic limit of the scaffolds, the necks between microspheres of adjacent layers broken, the microspheres displaced and misaligned along the centre's axis, finally leading to the sudden collapse of the scaffold structure (Figure 7D). The anisotropic mechanical behaviour observed with respect to the testing axis may be explained by considering the combination of thermal and solvent vapours sintering techniques to fabricate the layers and to assemble the 3D scaffolds, respectively. Indeed, the change of transparency of the sample during layers fabrication (not shown), indicated that microspheres melted completely, and therefore sintering occurred homogeneously through the entire neck section. Conversely, the solvent sintering plasticized adjacent microspheres starting from their surface, while solvent evaporation and microspheres volume contraction may induce the formation of tiny porosity inside connecting necks. Taking into the account these aspects, when tested along layers axis (x-axis), scaffolds have higher capability to sustain compression if compared to z-axis. Korpela *et al.* (2013) fabricated PCL scaffolds using fused deposition modelling having 30-40 % porosity, 0º/90º strand orientation and pore size of either 400 or 550 µm. In agreement with our results, the authors reported up to 40% decrease of compression modulus when tested along z-axis, if compared to x-axis. The different trend observed for the σ_Y values of IP and LP scaffolds along the x-axis and z-axis is ascribable to the different behaviour of the samples, as the IP scaffolds experienced higher bending than the LP one (compare Figures 7E and F). Noteworthy, the compressive mechanical properties of cubic-shaped PCL scaffolds were in the range of the values reported in the literature for hard TE applications (Hollister 2005, Salerno *et al.* 2017).

The biocompatibility properties of the scaffolds were evaluated both *in vitro* and *in vivo*. *In vitro* tests were carried out on scaffolds displaying square configuration with the microsphere's centres located onto four corners and showed that the scaffolds supported cell

adhesion and proliferation (Figure 8). Cell adhesion onto the scaffolds depends on different factors, mainly cell/material interaction and seeding procedure. As reported by other studies, static seeding may result in low cell adhesion as the seeding suspension can flow outside through the aligned pores, leaving most of the cells adherent to the bottom of the culture plate (Salerno *et al.* 2020b). The highest cell adhesion and proliferation observed for the CTR, (Figure 8A) is in agreement with literature studies on similar *in vitro* cell culture systems and ascribable to the enhanced cell-material interaction as well as nutrients transport of CTR, if compared to PCL scaffolds (Buckley and O`Kelly, 2010; Salerno et al. 2013). Regarding the PCL-HUVECs interaction *in vitro* Reid *et al.* (2020) modulated the morphology and structure of electrospun PCL scaffolds to find the best condition for endothelial cell proliferation and angiogenic expression. Others studies proposed the modification of fibrous PCL scaffolds with either fusion protein VEGF-HGFI (Zhao *et al.* 2016) or poly(glycerol sebacate) (Sant *et al.* 2011) to enhance HUVEC response. Furthermore, NaOH surface activation of PCL based scaffolds exerted a positive effect on HUVEC adhesion by increasing the number of OH groups onto the scaffold surface and, therefore, the adsorption of culture medium proteins mediating cell adhesion (Gupta *et al.* 2019, Richbourg *et al.* 2019, Rossi *et al.* 2016). It is noteworthy that, also in the case of neat PCL scaffolds (- NaOH) HUVECs proliferation increased over culture time and the normalized cell number values were higher than those obtained for + NaOH scaffolds at 7 and 11 days (Figure 8B). Taking into account these results we selected -NaOH scaffolds for the *in vivo* trials.

Implantation in a mouse subcutaneous pocket model was carried out to investigate if the geometrically-inspired design of microsphere-based scaffolds was capable to stimulate the host biological response and promote cell invasion as well as the onset of a newly formed vascular network inside the scaffold. As the oxygen amount required for cell survival is limited to a short (200 μm) distance from the supplying blood vessel, long-term survival and function of thick

engineered constructs are critically dependent on the successful development of new blood vessels (Choi *et al.* 2013, Gupte *et al.* 2018, Tang *et al.* 2020). In this work, we assess the role of scaffold microarchitecture, namely the LP and IP square configuration of Figures 3A and E, respectively on vascularization. To this purpose, we used a 3D imaging protocol as it allows the morphometric assessment of angiogenic processes, enabling the evaluation of the vascular network inside the scaffolds by measuring the overall vascularization percentage, the vascular penetration depth and the average vessels diameter (Palladino *et al.* 2021). Samples were, therefore, retrieved after 21 days following circulatory system perfusion with a radio-opaque polymer to enhance the contrast between the vessels, the scaffold material and surrounding tissues. As shown in Figures 9A-C, scaffold vascularization was not significantly affected by the characteristics of the porous structure of the scaffolds. This unexpected result can be explained by considering that blood vessels growth into the scaffolds not only depended on local vascularization at the site of implantation, but mostly on its spatial organization. In fact, in our *in vivo* campaign we observed the preferential growth of blood vessels from the lateral sides of the scaffolds. As previously commented, both tested scaffolds have similar pore structural features on the four lateral sides, with pore size equals to 150 µm ca. Therefore, the effect of the pore architecture transversally to the layers plane had a minor effect on vascularization. This consideration was also supported by the results of the spatial distribution of blood vessels, reported in Figure 9B, that indicated higher values in the scaffold region close to the external vascularization. The role of scaffolds porosity and pore size on *in vivo* blood vessels ingrowth has been deeply studied in scientific literature (Choi et al. 2013, Gupte et al. 2018, Mehdizadeh et al. 2013, Tang et al. 2020, Zieber et al. 2014). Gupte et al. (2018) fabricated nanofibrous poly (L-lactic acid) (PLLA) scaffolds with uniform, spherical, interconnected and well-defined pore sizes by using a thermally-induced phase separation and porogen leaching technique. The scaffolds were used to evaluate the effect of pores size, in the

ranges of 60-125, 125-250, 250-425, and 425-600 μm, on bone marrow stromal cell fate and vascularized bone formation during subcutaneous implantation in mice. In agreement with our results, the authors observed that scaffold pores larger than 125 μm were necessary to promote endochondral ossification and blood vessels penetration (Gupte et al. 2018). Similar results were obtained by Choi *et al.* (2013) that also demonstrated that scaffolds with small pore sizes favoured the formation of smaller blood vessels at higher densities and poor penetration depth, while larger blood vessels at lower densities developed deeply in scaffolds with large pore sizes. Most importantly, the integration of microchannels inside scaffolds structure may induce greater vessel density, complete tissue infiltration throughout the construct and the formation of functional blood vessels connected to the animal's cardiovascular system (Tang et al. 2020). We can, therefore, conclude that capability of microsphere-based scaffolds with geometrically-inspired architecture to support tissue regeneration stems from the combination of microstructural parameters of the scaffolds together with the amount, spatial organization, and structure of the pre-existing vasculature at the site of implantation. Even if the different designs reported in this work did not focus on specific TE purposes, they represent a proof of concept on the potential scaffold design capabilities of our manufacturing process. Besides, the use of PCL as building material and the pore structure features and mechanical properties evidenced by prepared samples suggested their potential application for load bearing tissues, such as bone and osteochondral tissue (Piard *et al.* 2019; Choe *et al.* 2022). The possible integration of drug delivery systems within PCL microspheres scaffolds will be studied further to assess the effect of spatial and temporal controlled delivery of biomolecules on new tissue growth and morphogenesis.

5 Conclusions

This work reported a feasible approach combining microfluidic emulsion for microspheres production and soft lithography for microsphere patterning suitable to fabricate PCL microspheres sintered scaffolds featured by an orderly architecture and geometrically-inspired design. Even if the process required multiple fabrication steps and time-consuming protocols for layers design, sintering and assembly, the final scaffolds display in-silico engineered morphological and microstructural features that, in our knowledge, have never been achieved before. This modular approach can be therefore used to design scaffolds displaying biomimetic morphological and architectural features observed in highly complex native tissues, like bone and osteochondral tissue. For instance, by sintering PCL microspheres layers featuring different designs it is possible to create porosity and pore size gradients to meet the microarchitectural requirements of bone and cartilage regions of osteochondral scaffolds (Lopa and Madry, 2014). Furthermore, the mild solvent sintering protocol used for layers bonding may enable the incorporation of biomolecules delivery carriers and studying the synergic role of 3D architecture and biomolecules delivery on *in vitro* and *in vivo* tissue growth and morphogenesis. The accuracy of design features and the excellent layer alignment and sintering resulted in PCL scaffolds with compression properties significantly higher than those obtained in other literature works for scaffolds prepared by the random assembly of PCL microspheres. Besides, we demonstrated that these scaffolds hold proper cells adhesion and proliferation capabilities supporting blood vessels ingrowth and tissue integration once implanted in the host organism. However, variation of scaffold design features and/or implantation site will be necessary to test the effect of scaffold internal characteristics on the extent of vascularization.

Ethical statement

All animal experiments were performed following the guidelines of the European Communities. Council Directive 2010/63/EU.

Acknowledgements

Aurelio Salerno acknowledges Raffaele Vecchione and Gabriele Pitingolo for their support to the micromilling setup as well as Valentina Mollo for MicroCT and SEM technical assistance.

References

Bernassau A L, MacPherson P G A, Beeley J, Drinkwater B W and Cumming D R S 2013 *Biomed. Microdevices* **15** 289.

Bittner S M, Guo J L and Mikos A G 2018 *Bioprinting* **12** e00032.

Borden M, Attawia M, Khan Y, El-Amin S F and Laurencin C T 2004 *J. Bone Joint Surg.* **86-B** 1200.

Buckley C T and O'Kelly K U 2010 *J. Mater. Sci. Mater. Med.* **21** 1731.

Cai W and Piestun R 2006 *Appl. Phys. Lett.* **88** 111112.

Causa A, Filippone G, Acierno D, Domingo C and Salerno A 2015 *Macromol. Chem. Phys.* **216** 49.

Chen J, Huang D, Wang L, Hou J, Zhang H, Li Y, Zhong S, Wang Y, Wu Y and Huang W 2020 *J. Colloid Interf. Sci.* **574** 162.

Choe R, Devoy E, Kuzemchak B, Sherry M, Jabari M, Packer J D and Fisher J P 2022 *Biofabrication* **14** 025015.

Choi S, Cheong I W, Kim J and Xia Y 2009 *Small* **5** 454.

Choi S, Zhang Y, MacEwan M R and Xia Y 2013 *Adv. Health. Mater.* **2** 145.

de Alteriis R, Vecchione R, Attanasio C, De Gregorio M, Porzio M, Battista E and Netti, P A 2015 *Sci. Rep.* **5** 12634.

Dormer N H, Singh M, Wang L, Berkland C J and Detamore M S 2010 *Ann. Biomed. Eng.* **38** 2167.

Fahimipour F, Rasoulianboroujeni M, Dashtimoghadam E, Khoshroo K, Tahriri M, Bastami F and Tayebi L 2017 *Dent. Mater.* **33** 1205.

Feng D, Weng D and Wang J 2019 *J. Colloid Interf. Sci.* **548** 312.

Gallego D, Ferrell N, Sun Y and Hansford D J 2008 *Mater. Sci. Eng. C.* **28** 353.

Guan J, He H, Lee L J and Hansford D J 2007 *Small* **3** 412.

Gupta V, Tenny K M, Barragan M, Berkland C J and Detamore M S 2016 *J. Biomater. Appl.* **31** 328.

Gupta D, Singh A K, Kar N, Dravid A and Bellare J 2019 *Mater. Sci. Eng. C* **98** 602.

Gupte M J *et al.* 2018 *Acta Biomater.* **82** 1.

Hollister S J 2005 *Nat. Mater.* **4** 518.

Hoogenboom J P, Vossen D L J, Faivre-Moskalenko C, Dogterom M and van Blaaderen A 2002 *Appl. Phys. Lett.* **80** 4828.

Kant R J and Coulombe K L K 2018 *Acta Biomater.* **69** 42.

Khoshroo K, Kashi T S J, Moztarzadeh F, Tahriri F, Jazayeri H E and Tayebi L 2017 *Mater. Sci. Eng. C* **70** 586.

Kim C M, Lee H B, Kim J U and Kim G M 2017 *J. Micromech. Microeng.* **27** 125018.

Korpela J, Koddari A, Korhonen H, Malin M, Närhi T and Seppälä J 2013 *J. Biomed. Mater. Res. Part B Appl. Biomater.* **101B** 610.

Jabbarzadeh E, Deng M, Lv Q, Jiang T, Khan Y M, Nair L S and Laurencin C T 2012 *J. Biomed. Mater. Res. Part B: Appl. Biomater.* **100B** 2187.

Jaklenec A, Wan E, Murray M E and Mathiowitz E 2008a *Biomaterials* **29** 185.

Jaklenec A, Hinckfuss A, Bilgen B, Ciombor D M, Aaron R and Mathiowitz E 2008b *Biomaterials* **29** 1518.

Jacob S, Nair A B, Patel V and Shah J 2020 *AAPS Pharm. Sci. Tech.* **21** 220.

Jiang T, Nukavarapu S P, Deng M, Jabbarzadeh E, Kofron M D, Doty S B, Abdel-Fattah W I and Laurencin C T 2010 *Acta Biomater.* **6** 3457.

Levato R, Visser J, Planell J A, Engel E, Malda J and Mateos-Timoneda M 2014 *Biofabrication* **6** 035020.

Li X, Wang T, Zhang J, Yan X, Zhang X, Zhu D, Li W, Zhang X and Yang B 2010 *Langmuir* **26** 2930.

Li H *et al.* 2021 *Front. Bioeng. Biotechnol.* **9** 662381.

Liu H, Ahlinder A, Yassin M A, Finne-Wistrand A and Gasser T C 2020 *Mater. Des.* **188** 108488.

Lopa S and Madry H 2014 *Tissue Eng. Part A* **20** 2052.

Lu H H, El-Amin S F, Scott K D and Laurencin C T 2003 *J. Biomed. Mater. Res.* **64A** 465.

Luciani A, Coccoli V, Orsi S, Ambrosio L and Netti P A 2008 *Biomaterials* **29** 4800.

Luciani A, Guarino V, Ambrosio L and Netti P A 2011 *J. Mater. Sci. Mater. Med.* **22** 2019.

Lv Q, Nair L and Laurencin C T 2009 *J. Biomed. Mater. Res.* **91A** 679.

Matai I, Kaur G, Seyedsalehi A, McClinto A and Laurencin C T 2020 *Biomaterials* **226** 119536.

Mehdizadeh H, Sumo S, Bayrak E S, Brey E M and Cinar A 2013 *Biomaterials* **34** 2875.

Moon S, Cheong I W and Choi S 2014 *Colloids Surf. A Physicochem. Eng. Asp.* **454** 84.

Muto H, Kimata K, Murata K, Daiko Y, Matsuda A and Sakai M 2009 *Mater. Sci. Eng. B* **161** 193.

Palladino P, Pizzoleo C, Mavaro I, Lucini C, D'Angelo L, de Girolamo P and Attanasio, C 2021 *Ann. Anat.* **37** 151727.

Pedram P, Mazio C, Imparato G, Netti P A and Salerno A 2021 *ACS Appl. Mater. Interfaces* **13** 9589.

Petrie Aronin C E, Sadik K W, Lay A L, Rion D B, Tholpadhy S S, Ogle R C and Botchwey E A 2009 *J. Biomed. Mater. Res.* **89A** 632.

Piard C, Baker H, Kamalitdimov T and Fisher J 2019 *Biofabrication* **11** 025013.

Reid J A, McDonald A and Callanan A 2020 *Plos One* **15** e0240332.

Richbourg N R, Peppas N A and Sikavitsas V I 2018 *J. Tissue Eng. Regen. Med.* **13** 1275.

Rose M A, Vinod T P and Morin S A 2018 *J. Mater. Chem. C.* **6** 12031.

Rossi L, Attanasio C, Vilardi E, De Gregorio M and Netti P A 2016 *J. Mater. Sci. Mater. Med.* **27** 107.

Ryu W, Min S W, Hammerick K E, Vyakarnam M, Greco R S, Prinz F B and Fasching RJ 2007 *Biomaterials* **28** 1174.

Salerno A, Levato R, Mateos-Timoneda M, Engel E, Netti P A and Planell J 2013 *J. Biomed. Mater. Res. Part A* **101A** 720.

Salerno A, Diéguez S, Diaz-Gomez L, Gómez-Amoza J L, Magariños B, Concheiro A, Domingo C, Alvarez-Lorenzo C and García-González C A 2017 *Biofabrication* **9** 035002.

Salerno A, Cesarelli G, Pedram P and Netti P A 2020a *J. Clin. Med.* **8** 1816.

Salerno A, Leonardi A, Pedram P, Di Maio E, Fanovich A and Netti P A 2020b *Mater. Sci. Eng. C* **109** 110518.

Salerno A and Netti P A 2021 *Front. Bioeng. Biotechnol.* **9** 682133.

Samorezov J E and Alsberg E 2015 *Adv. Drug Deliv. Rev.* **84** 45.

Sant S, Hwang C M, Lee S and Khademhosseini A 2011 *J. Tissue Eng. Reg. Med.* **5** 283.

Sawkins M J, Mistry P, Brown B N, Shakesheff K M, Bonassar L J and Yang J 2015 *Biofabrication* **7** 035004.

Seul M, Chau C W, Huang H, Banerjee S, Yang J and Hong Y 2008 *U.S. Patent N.* **US007335153B2**.

Shahin-Shamsabadi A, Hashemi A and Tahriri M 2018 *J. Med. Biol. Eng.* **38** 359.

Shi X, Wang Y, Varshney R R, Ren L, Gong Y and Wang D 2010 *Eur. J. Pharm. Sci.* **39** 59.

Singh M, Sandhu B, Scurto A, Berkland C and Detamore M S 2010 *Acta Biomater.* **6** 137.

Sodha S, Wall K, Redenti S, Klassen H, Young M J and Tao S L 2011 *J. Biomater. Sci.* **22** 443.

Sonnaert M, Papantoniou I, Luyten F P and Schrooten J 2015 *Tissue Eng. Part C* **21** 519.

Tang F, Manz X D, Bongers A, Odell R A, Joukhdar H, Whitelock J M, Lord M S and Rnjak-Kovacina J 2020 *ACS Biomater. Sci. Eng.* **6** 1476.

Tarafder S, Kock A, Jun Y, Chou C, Awadallah M R and Lee C H 2016 *Biofabrication* **8** 025003.

Tedesco M T, Di Lisa D, Massobrio P, Colistra N, Pesce M, Catelani T, Dellacasa E, Raiteri R, Martinoia S and Pastorino L 2018 *Biomaterials* **156** 159.

Xie Y, Yang Y, Kang X, Li R, Volakis L I, Zhang X, Lee L J and Kniss D A 2009 *Biotechnol. Prog.* **25** 535.

Yang Y, Basu S, Tomasko D L, Lee J and Yang S 2005 *Biomaterials* **26** 2585.

Wang Y, Shi X, Ren L, Wang C and Wang D 2009 *Mater. Sci. Eng. C* **29** 2502.

Wang Y, Shi X, Ren L, Yao Y and Wang D 2010 *J. Biomater. Sci.* **21** 1227.

Watanabe T, Ono T and Kimura Y 2011 *Soft Matter* **7** 9894.

Zhao L *et al.* 2016 *Adv. Health. Mater.* **5** 2376.

Zhao N, Lv Z, Ma J, Zhu C and Li Q 2019 *Eur. Polym. J.* **110** 31.

Zhou Z, Yao Q, Li L, Zhang X, Wei B, Yuan L and Wang L 2018 *Med. Sci. Monit.* **24** 6934.

Zieber L, Or S, Ruvinov E and Cohen S 2014 *Biofabrication* **6** 024102.

Table 1: Porosity and pore size values of PCL microsphere-sintered scaffolds as a function of microspheres patterning, compared with the correspondent virtual model's porosity and pores size values. Porosity values were obtained by gravimetric measurements combined with geometrical calculation and taking into the account PCL bulk density of 1.145 g/cm^3. Pore size values were obtained by Image J analysis of SEM pictures of the scaffolds. The pore sizes of the virtual models and correspondent scaffolds were classified based on the size range into three main types: type I pores were the smallest pores equal to 77 µm of the hexagonal configuration; type II pores were intermediate pores equal to 207 µm of square configuration with the microsphere's centres located onto four corners, or equal to 210 µm of octagonal, dodecagonal and dodecagonal plus hexagonal configurations; type III pores were the largest pores equal to 500 µm of IP configurations, or equal to 810 µm and 1430 µm of octagonal and dodecagonal configuration, respectively.

Figure 1: Different steps used for the fabrication of the scaffolds. Step 1: fabrication of PCL microspheres by fluidic emulsion of a CP consisting of water solution of Tween 20 (0.1 v/v%) and PVA (0.5 w/v%), and a DP consisting of 10 w/v% PCL in DCM. The emulsion was carried out at Q_{CP} = 9 mL/min and Q_{DP} = 90 µL/min, to achieve microsphere of Φ = 500 µm diameter. Step 2: patterned PDMS moulds were fabricated via soft lithography and used to create PCL microsphere layers with pre-defined geometries. The moulds were obtained starting from a PMMA master prepared by micromilling technique followed by a replica moulding process. Step 3: PCL microsphere layers were obtained by pouring the microspheres onto the patterned moulds followed by thermal sintering at 64 °C for 7 minutes. Step 4: 3D scaffolds were assembled by the alignment and stacking of up to six sintered layers of PCL microspheres. The layers were subsequently sintered by a solvent vapour treatment carried out by using a 30/70 v/v % DCM/EtOH mixture for 2 minutes on each side.

Figure 2: (A) Effect of processing conditions (e.g. concentration of PCL in DCM in the 1-10 wt% range and Q_{CP} in the 4-18 mL/min range) on PCL microspheres Φ prepared at Q_{DP} = 90 µL/min. Morphology of the surface (B, C) and cross-section (D) of PCL microspheres prepared from 10 % w/v solution at Q_{CP} = 9 mL/min and Q_{DP} = 90 µL/min.

Figure 3: CAD images showing the virtual models of the different scaffolds prepared in this work: LP scaffolds were obtained by (A) square configuration with the microsphere's centres located onto four corners and by (B) closed-packed hexagonal configuration; HP scaffolds were obtained by (C) octagonal and by (D) dodecagonal configurations; IP scaffolds were obtained by (E) square configuration with the microsphere's centres located onto three corners and by (F) the combination of hexagonal and dodecagonal configurations.

Figure 4: Effect of design configuration on the morphology of sintered layers as assessed by SEM analysis. (A, B) hexagonal, (C) square; (D-F) octagonal and (G-K) dodecagonal configuration.

Figure 5: Effect of design configuration on the morphology of 3D PCL scaffolds as assessed by SEM analysis. (A) and (B) square configuration with the microsphere's centres located onto four and three corners, respectively; (C,D) octagonal; (E,F) dodecagonal combined with hexagonal configuration; (G,H) side surface of the scaffold prepared from octagonal configuration; (K) cross-section image of the scaffold prepared from octagonal configuration.

Figure 6: 3D reconstructions of different scaffolds obtained by MicroCT analysis: (A) square configuration with the microsphere's centres located onto four corners; (B) hexagonal configuration; (C) octagonal configuration; (D) dodecagonal configuration; (E) square configuration with the microsphere's centres located onto three corners; (F) dodecagonal combined with hexagonal configuration.

Figure 7: Static compression properties of scaffolds featuring square configuration with the microsphere's centres located onto four (IP) and three corners (IP) as assessed by MicroCT

tests: (A) representative $\sigma \div \varepsilon$ curves of scaffolds and (B) resulting compression parameters (e. g. E, σ_Y and ε_Y); 3D reconstructions of (C,E) LP and (D,F) IP scaffolds at the end of the static compression test, as a function of compression axis.

Figure 8: Cell material interaction between HUVEC cells and PCL scaffolds (n=3). The graph in (A) displays the results of a cell viability assay reported as number of viable cells at different time points onto the raw scaffold (-NaOH), the surface activated scaffold (+ NaOH) and the petri dish used as control (CTR). The graph in (B) displays the relative fold increase 6 hours post-seeding for the three samples. Pictures in C and D show confocal images of HUVECs adhered onto the surface and onto the neck of the scaffold (+NaOH type) at 11 days of *in vitro* culture. Actin was stained with Phalloidin-488 (red) while nucleus was stained with DRAQ5 (green).

Figure 9: Results of the analysis of scaffolds vascularization by MicroCT performed on Microfil perfused explants. (A) Vessel volume within the scaffolds (n=5) is expressed in mm^3; (B) spatial distribution of vessel volume as a function of the distance from the main external vasculature (from A to C); (C) distribution of the size of blood vessels within the implants. The inset in Figure 9A show a 3D reconstruction of blood vessels morphology and spatial distribution as achieved by MicroCT analysis of microfil perfused LP sample. (D-E) Histological images of scaffold sections (LP of Figure 3A) implanted in a mouse subcutaneous pocket model and retrieved 21 days post-implantation. In panel (D) is displayed the host tissue integrated into the scaffold; in panel (E) details of both cellular and ECM components are shown while panel (F) highlights the vascular compartment of the newly formed tissue. The small red roundish particles are blood cells while the small dark roundish particles are residual Microfil components (lead) (n = 3).

Table 1

Configuration		**Low porosity (LP)**		**High porosity (HP)**		**Intermediate porosity (IP)**	
Coordination sphere number		6	8	4 and 5	5 and 6	4 and 6	6 and 7
CAD scaffolds features							
Overall porosity [%]		47.6	43.1	63.1	70.4	58.4	51.4
Pore diameter [µm]	Type I	/	77	/	77	/	77
	Type II	207	/	210	210	/	210
	Type III	/	/	810	1430	500	500
Measured scaffolds features							
Overall porosity [%]		41.7 ± 1.3	38.4 ± 1.1	60.2 ± 1.2	67.6 ± 1.4	54.8 ± 0.7	46.7 ± 0.8
Pore diameter [µm]	Type I	/	76.9 ± 1.8	/	70.5 ± 4.7	/	74.0 ± 6.1
	Type II	200.1 ± 7.7	/	196.8 ± 5.2	204.2 ± 18.8	/	199.9 ± 8.7
	Type III	/	/	790.9 ± 24.9	1373.5 ± 14.9	599.9 ± 24.2	508.7 ± 10.7

Figure 1

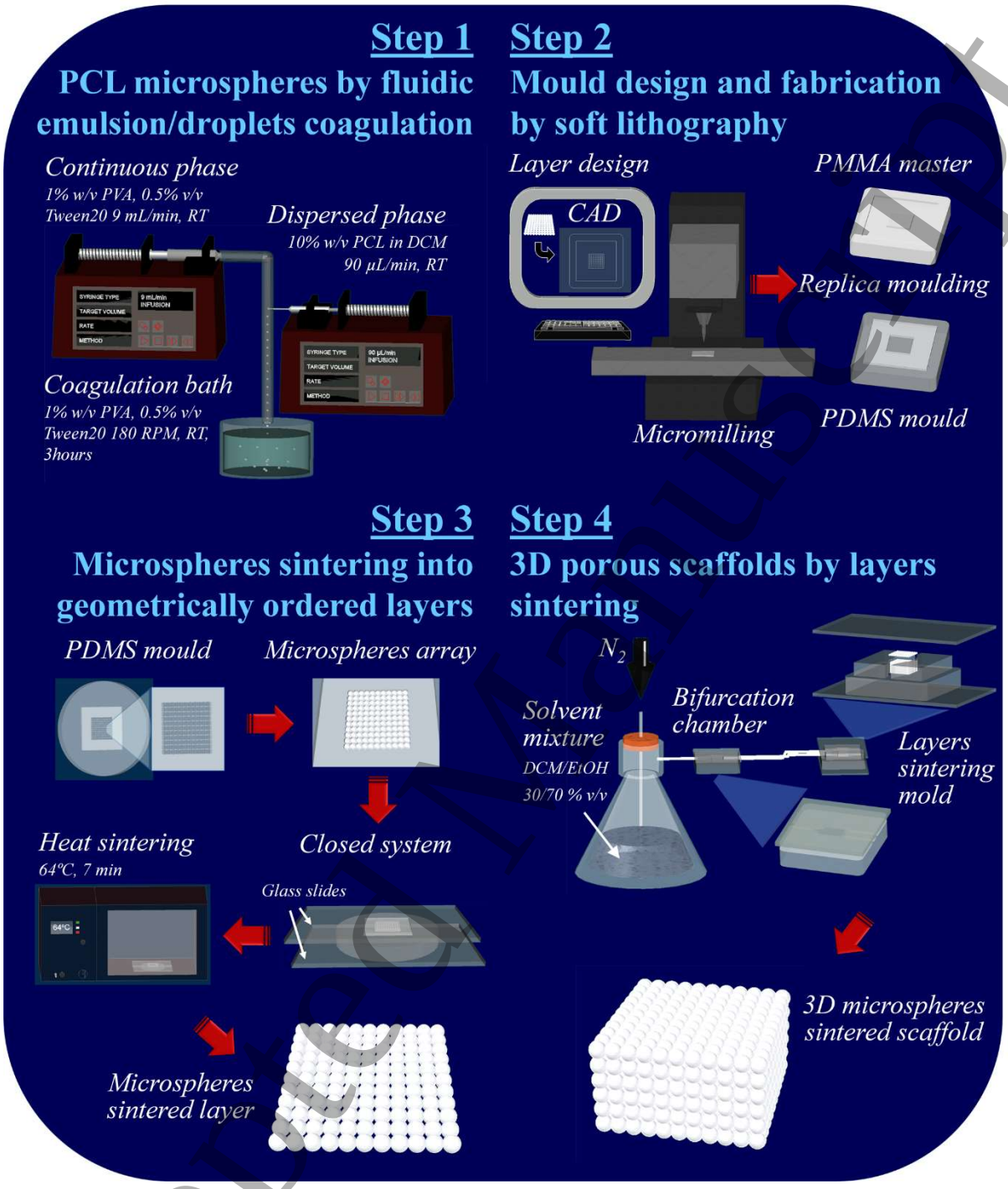

Figure 2

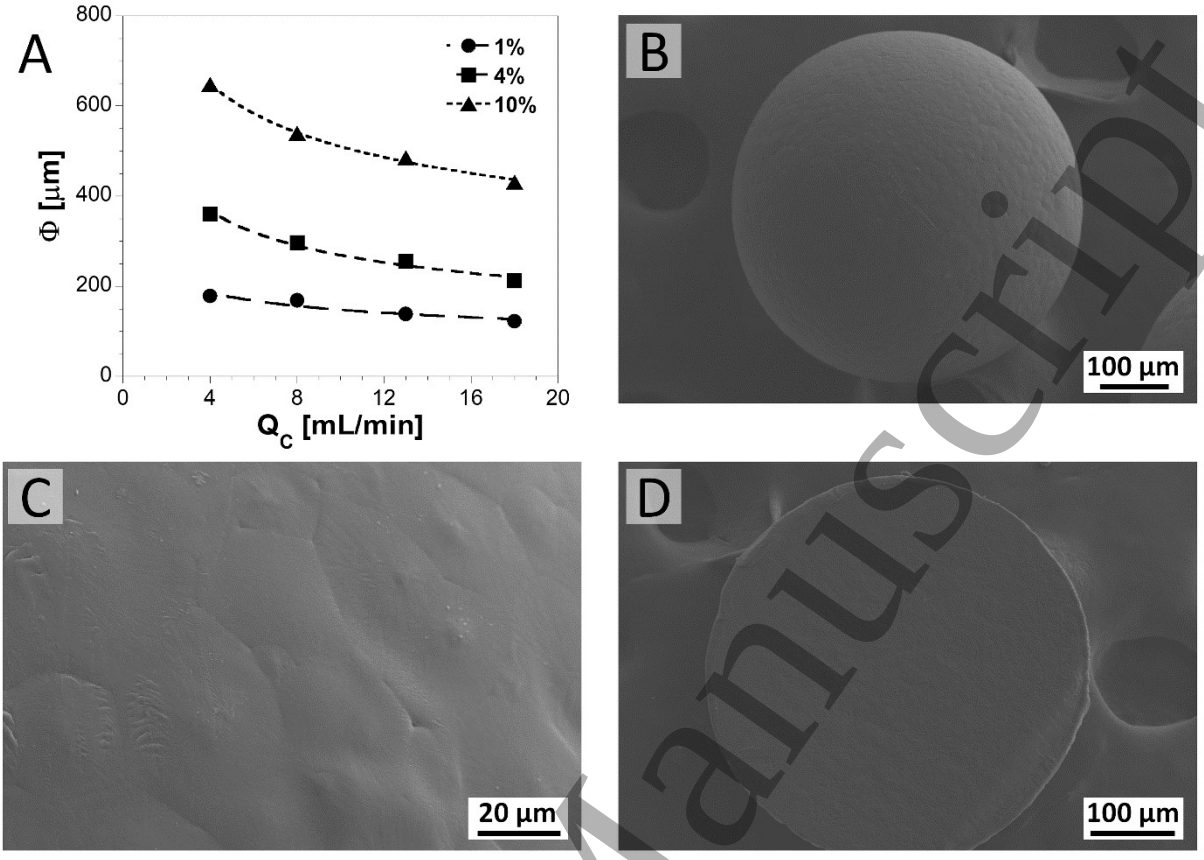

Figure 3

Configuration	Low porosity (LP)		High porosity (HP)		Intermediate porosity (IP)	
Coordination sphere number	6	8	4 and 5	5 and 6	4 and 6	6 and 7
Unit cell					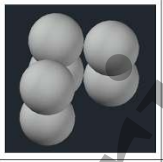	
Spheres array				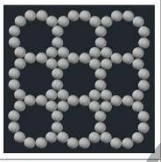		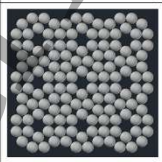
3D ordered scaffold		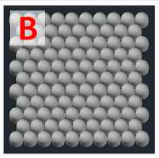	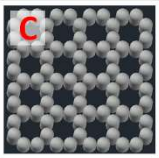	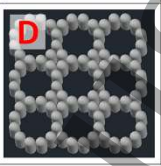	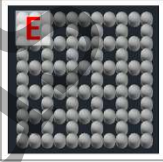	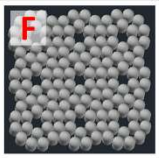

Figure 4

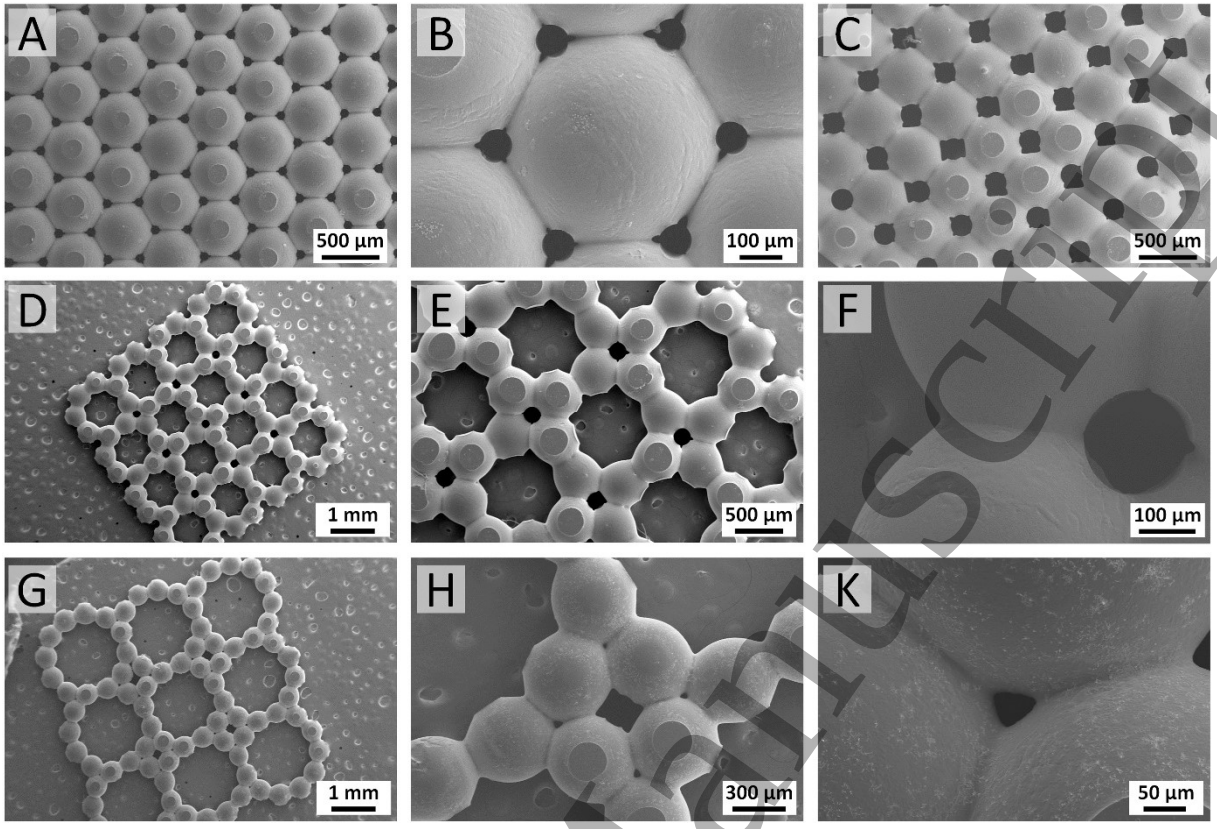

Figure 5

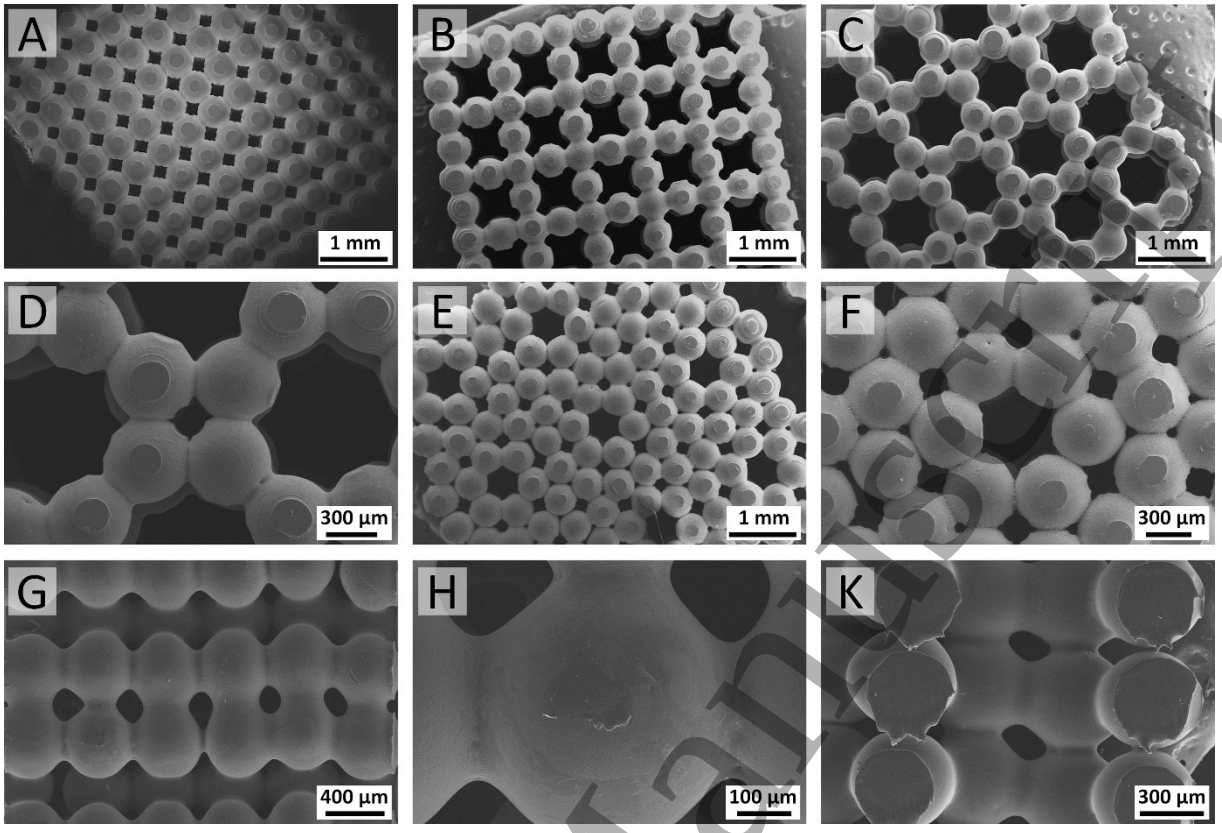

Figure 6

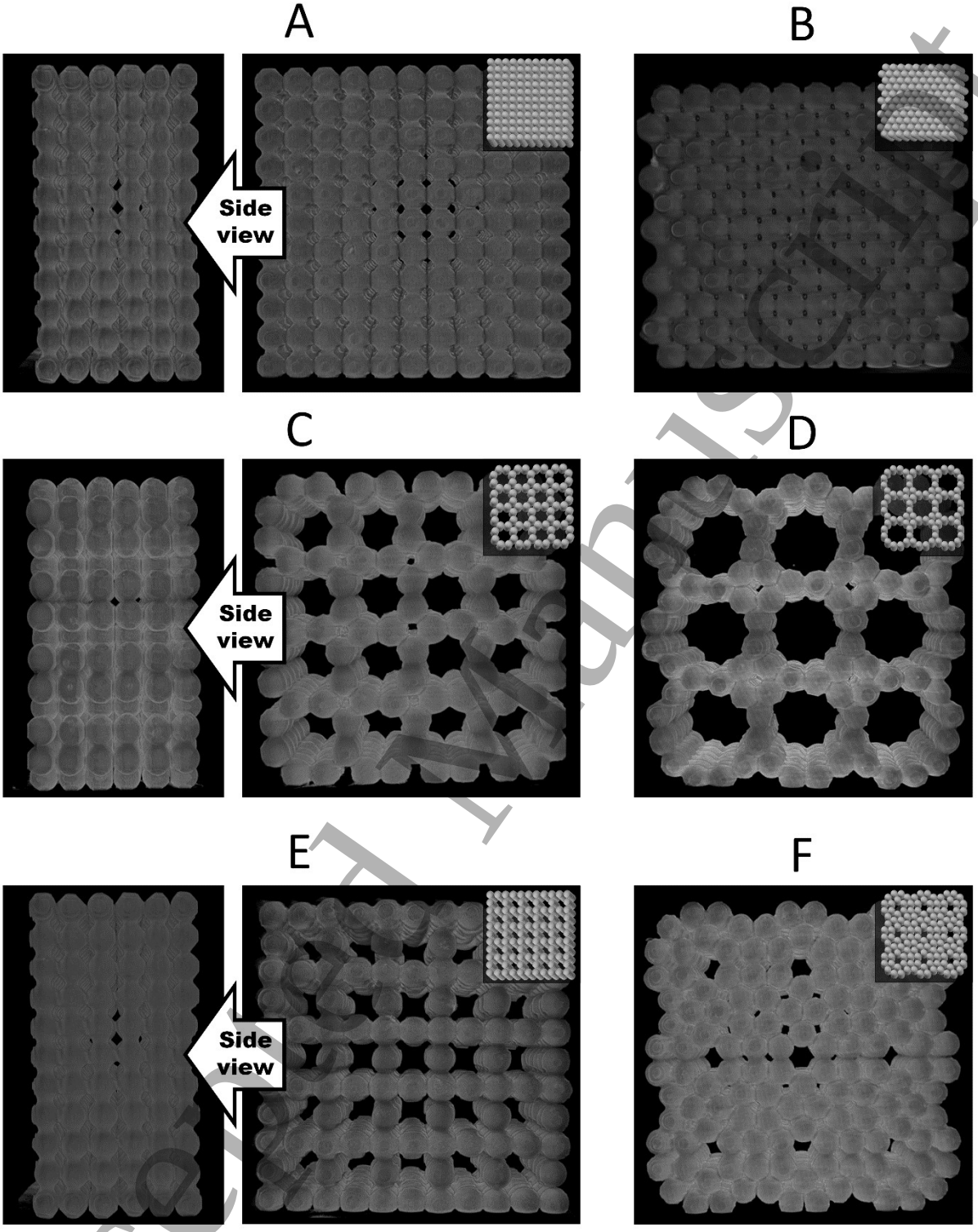

Figure 7

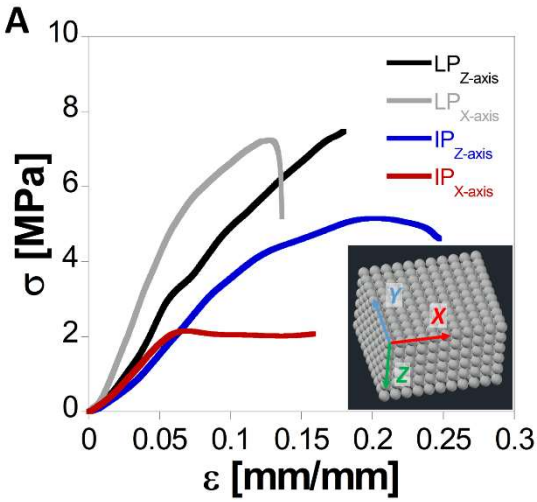

B

Scaffold type		LP	IP
E [MPa]	*Z-axis*	54.2 ± 9.9	33.7 ± 6.9
	X-axis	96.7 ± 15.2	43.3 ± 3.7
ε_Y [mm/mm]	*Z-axis*	0.09 ± 0.02	0.14 ± 0.02
	X-axis	0.06 ± 0.02	0.04 ± 0.01
δ_Y [MPa]	*Z-axis*	4.15 ± 0.46	3.2 ± 0.62
	X-axis	5.65 ± 0.93	1.56 ± 0.44

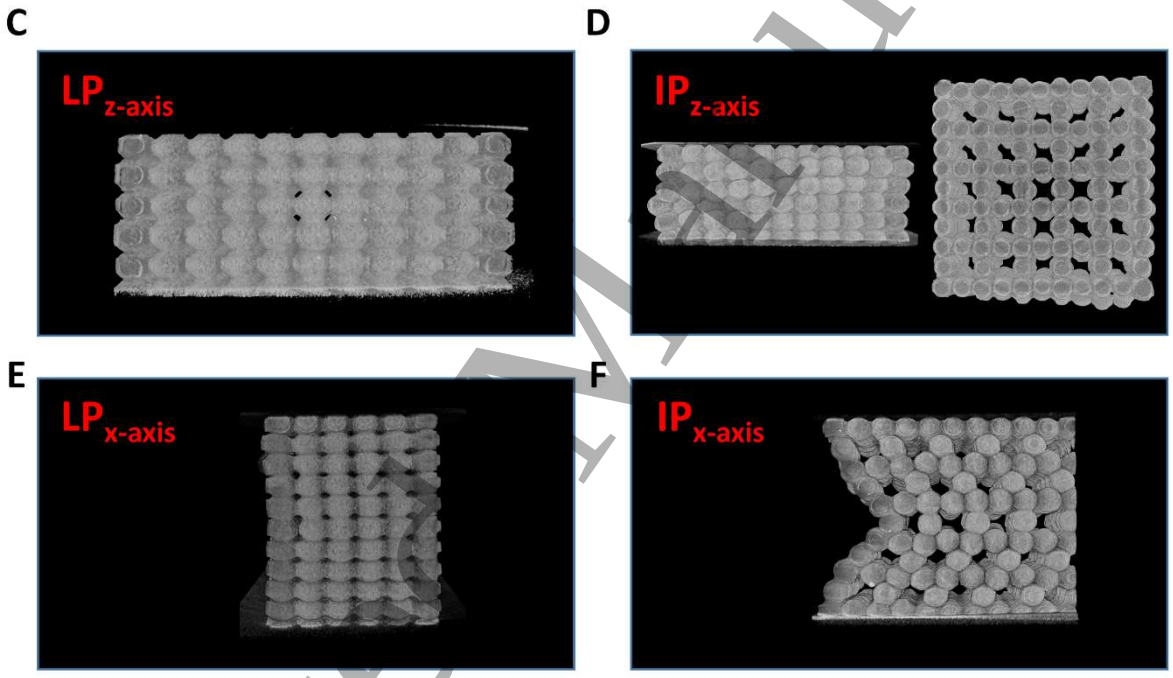

Figure 8

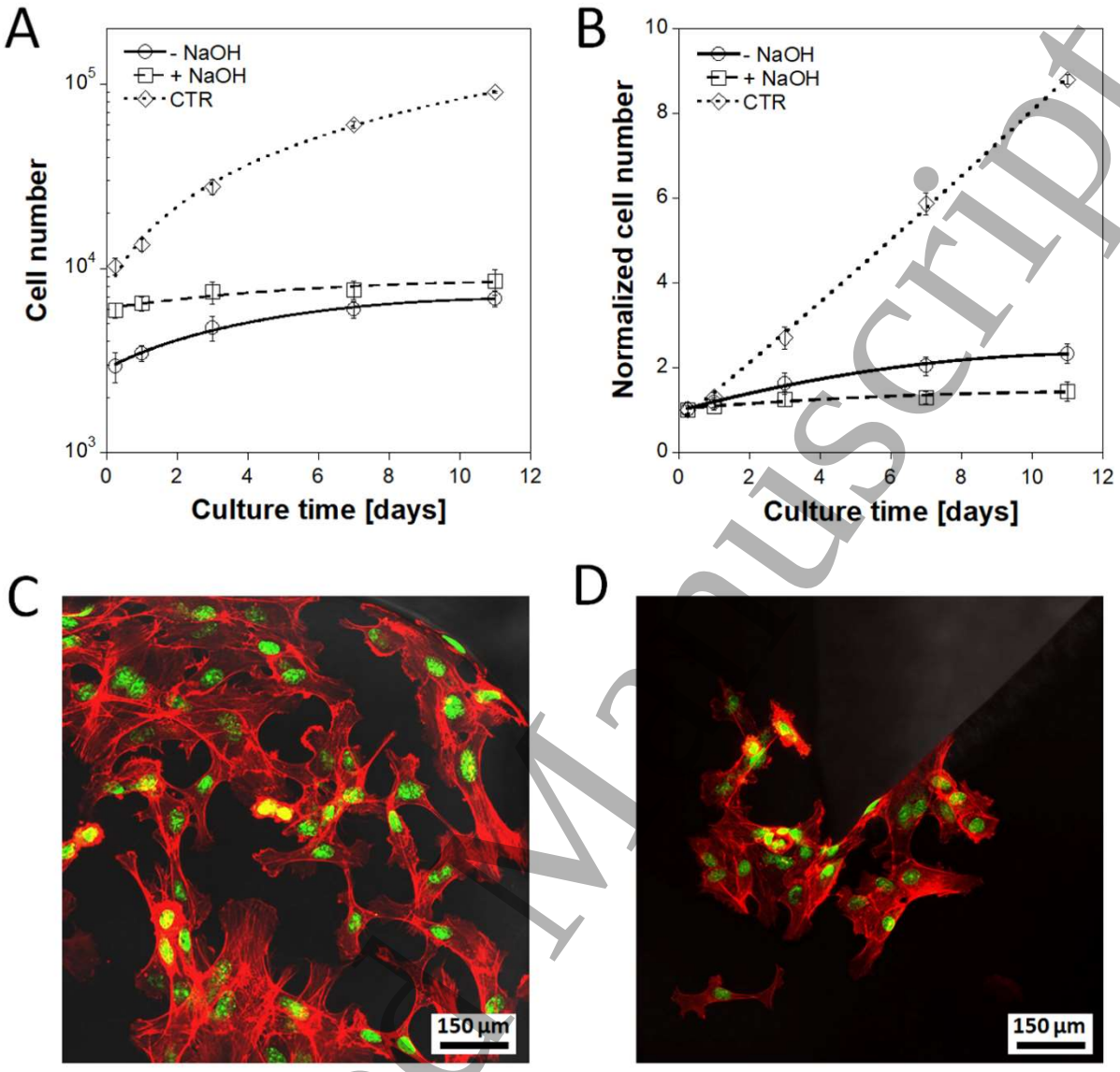

Figure 9